Supplementary Information

Decoding the counterintuitive role of electron transfer in photothermal ammonia synthesis over Ru/CeO$_2$ catalysts

1. Experimental Details

1.1. Catalyst Characterization

X-ray diffraction patterns (XRD) were collected on Rigaku Ultima III equipped with Cu Kα source. Transmission electron microscopy (TEM) images and energy dispersive spectroscopy mapping (EDS-mapping) were obtained from JEOL JEM-2010 and JEOL JEM-F200. Inductively couple plasma atomic emission spectrum (ICP-AES) was collected on Agilent 5800. UV-Visible adsorption spectrum was obtained on Shimadzu UV-3600. Catalyst samples were diluted with BaSO$_4$ to the same fold before test. Electron paramagnetic resonance (EPR) was collected on Bruker EMX-500 10/12 at room temperature in air. Photoluminescence spectroscopy (PL) was collected on Shimadzu RF-5301 PC with 0.5 nm resolution scanning at 200 nm/min. A 300 nm laser was used as excitation source. Raman spectra were collected on Horiba Scientific, and a 325 nm UV laser was used. Temperature programmed reduction (H$_2$-TPR) was performed as follows. 100 mg sample was heated at 300 °C in Ar flow (30 mL/min) for 60 min at a ramp speed of 10 °C/min. After sample was cooled down to 50 °C, 10% H$_2$/Ar (30 mL/min) was introduced, and TCD signal was then collected from 50 °C to 800 °C at a ramp rate of 10 °C/min.

1.2. Preparation of Photoelectrode

Preparation method was according to previous reported work [1]. The Indium doped tin oxide (ITO) was cleaned by ultrasonication in DI water, absolute ethanol, and isopropanol for 15 min sequentially and dried at 60 °C. 5 mg catalyst was dispersed in a 1.5 mL mixture of DI water, isopropanol and Nafion solution (volumetric ratio = 1130:300:70) by ultrasonication for 30 min to ensure a homogenous dispersion. 10 μL of as-mentioned dispersion was added dropwise onto 1 cm^{-2} ITO glass and dried in air to form working electrode.

1.3. Photoelectrochemical Measurement

Photoelectrochemical measurement was executed on CHI600F electrochemical workstation, and a conventional three-electrode cell was used. A saturated calomel electrode (SCE) was used as reference electrode, Pt mesh electrode as counter electrode, and as-synthesized samples coated on ITO glass as working electrode. [2] Mott-Schottky plots and photocurrent response experiments were collected in the electrolyte of 0.1 M Na$_2$SO$_4$. For Mott-Schottky plots, 500, 1000, 1500, 2000, 2500 Hz were set as frequency values to gain the frequency-independent flat band potential. For photocurrent response experiments, A Xe lamp with 420 nm cut-off filter was used as light source for photocurrent response experiments, and 0.5 V bias versus SCE was applied.

1.4. Finite Difference Time Domain (FDTD) Simulation

The near field enhancement simulation was performed using FDTD method. For simulation, Ru nanoparticle was modelled as a sphere with 1.6 nm diameter and placed on CeO$_2$ sheet with 10 nm thickness. This model was built based on TEM images of reacted catalysts. The complex dielectric constant of Ru was taken from previous work [3] and calculated based on Drude model. [4] The complex refractive index of CeO_2 was obtained from reported work [5]. A z-polarized total-field scattering field (TFSF) source with wavelength range from 190 nm to 800 nm was used. A mesh override region with 0.08 nm cells was used to simulate. Periodic boundary condition was used along x and y axis, and perfect matched layer (PML) was used along z axis. Frequency domain field monitors were used to record electric field distribution, and power monitors behind nanoparticle and the light source were used to record the transmittance and reflectance cross-section.

1.5. Electron Density Difference Calculation

The Vienna Ab initio Simulation Package (VASP) [6] was used to perform density functional theory (DFT) calculation. A plane wave basis set with a cutoff energy of 450 eV and projector augmented wave (PAW) method represents the element core and valence electrons. The generalized gradient approximation with Perdew-Burke-Ernzerhof (GGA-PBE) exchange-correlation functional was used in all calculations. Geometry optimization was performed with force convergence of 0.05 eV/Å. 3 × 3 CeO_2 (200) supercell was constructed to exclude interaction between metal and a vacuum layer of 15 Å was added along z-axis. To describe intrinsic defects in CeO_2, which are well-known to lead to localized electrons on Ce ions neighbouring vacancies, DFT + U method was introduced, and a U correction of 4.5 eV [7] was applied to Ce 4f states. The calculation method of electron density difference is based on previously reported work with a modification. [8]

1.6. Calculation Method of Schottky Barrier Height (SBH) and Band Structure

To illustrate a specific band structure diagram to evaluate SBH, the Schottky model which negligible band bending occurs on metal after it contacts with semiconductor, was assumed. Equation used to calculate SBH were presented as follows. [9]

$$SBH = E_{Fs} - E_{Fm} + E_n$$

Where E_{Fs} is Fermi level of semiconductor, E_{Fm} is Fermi level of metal, and E_n is distance from fermi level of semiconductor to its conduction band minimum.

Equation for calculation of E_n can be further expressed as follows.

$$E_n = E_g - E'$$

Where E_g is band gap of semiconductor, E' is distance from fermi level of semiconductor to valence band maximum.

Equations for determination of band structure of semiconductor were presented as follows.

$$VBM = E_{Fs} - E'$$
$$CBM = VBM + E_g$$

Where VBM is valence band maximum, CBM is conduction band minimum.

Table S1. Ruthenium content determined by ICP and XRF.

Sample	ICP	XRF
Ru/Ce-C	2.9 wt%	3.1 wt%
Ru/Ce-R	3.5 wt%	3.4 wt%

Table S2. Ammonia synthesis performance comparison at ambient pressure.

Catalyst	Temperature (°C)	Production Rate ($\mu mol \cdot g^{-1} \cdot h^{-1}$)	Ref.
Pt_1-Pt_n/TiN	280	13	10
AuRu/MgO	350	48	11
Ru SACs/silicalite-1	360	5	12
Ru/$SrTiO_3$	400	31	13
Ru/P25	400	62	
Ru/Aluminate	400	32	
Ru/Aluminosilicate	400	23	
Ru/La_2O_3	400	300	14
Ru/MgO	400	316	
Ru/SiO_2	450	270	15
Ru/CeO_2-750	450	326	16
Ru/Ce-C	450	429	This study
Ru/Ce-R	450	189	This study

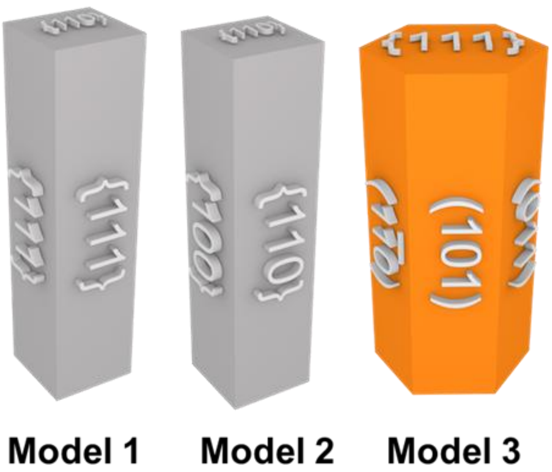

Fig S1. Facet distribution models of rod-shaped cerium.

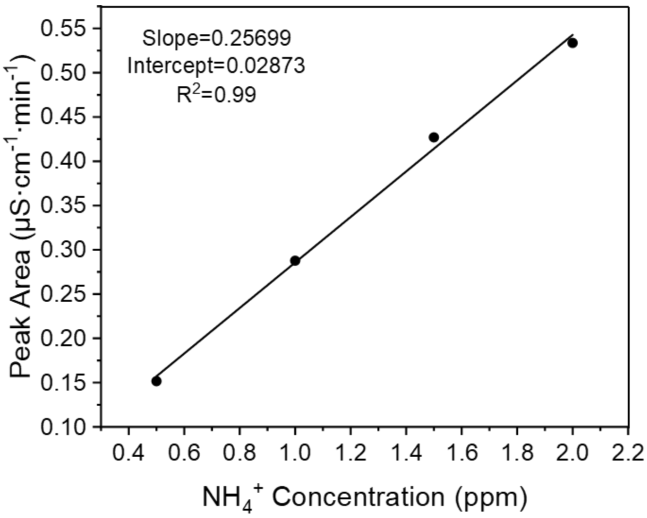

Fig S2. Standard calibration curve of ammonia.

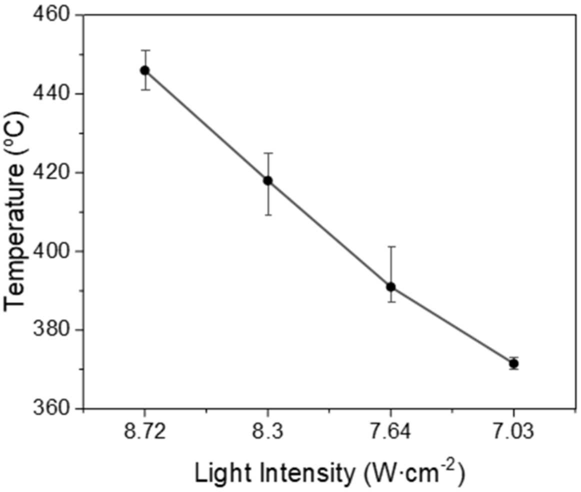

Fig S3. Temperature corresponding to light intensity for photothermal catalytic ammonia synthesis.

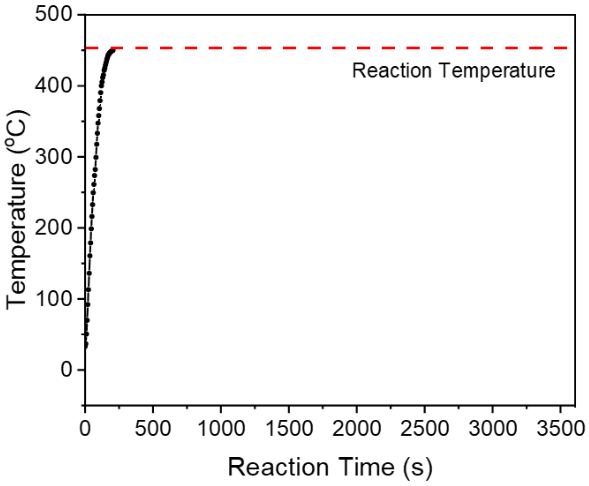

Fig S4. Temperature profile for thermal heating process until reaction temperature.

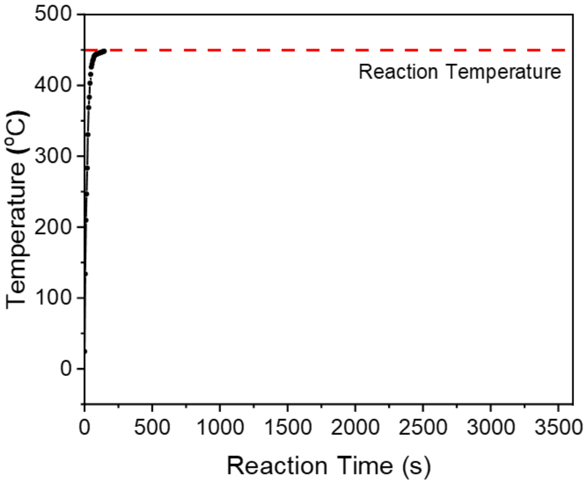

Fig S5. Temperature profile for photothermal heating until reaction temperature.

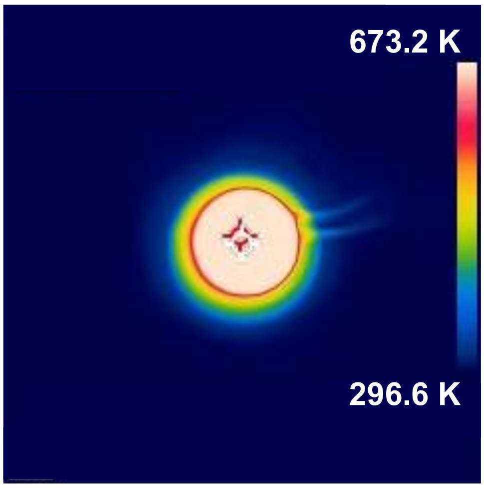

Fig S6. Thermal imaging for thermal catalytic condition.

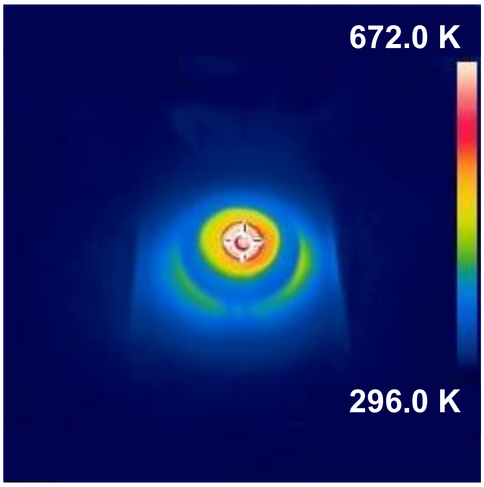

Fig S7. Thermal imaging (top view) of photothermal catalytic condition.

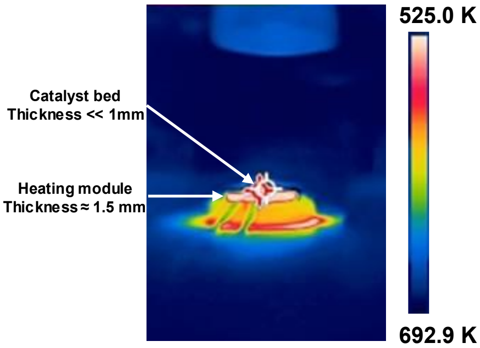

Fig S8. Thermal imaging (front view) of photothermal catalytic condition.

Note: As shown in Fig S6, 7, 8, Catalysts were both heated uniformly for thermal and photothermal condition. For thermal condition, loaded catalysts were heated by heating module while heating module was uniformly heated. For photothermal condition, loaded catalysts were heated by LSPR-induced heating. Only catalysts were greatly heated by light. However, thermal imaging around loaded catalysts was well distributed due to the uniform light adsorption and enough thin thickness of catalyst bed. Fig. S7, 8 were recorded at same heating condition but different perspectives. Due to the enough thin thickness of catalyst bed, thermal imaging only exhibits the uniform distribution for temperature of heating module. (Fig. S8) Even though the thickness of catalyst bed is below the resolution limit of thermal camera, considering the rapid heat transfer via thermal conduction and thin thickness below the penetration depth of light source, the temperature gradient inside catalyst bed was supposed to be far away from the scale of reaction temperature (400-500 °C). Therefore, the temperature gradient of catalyst bed was negligible.

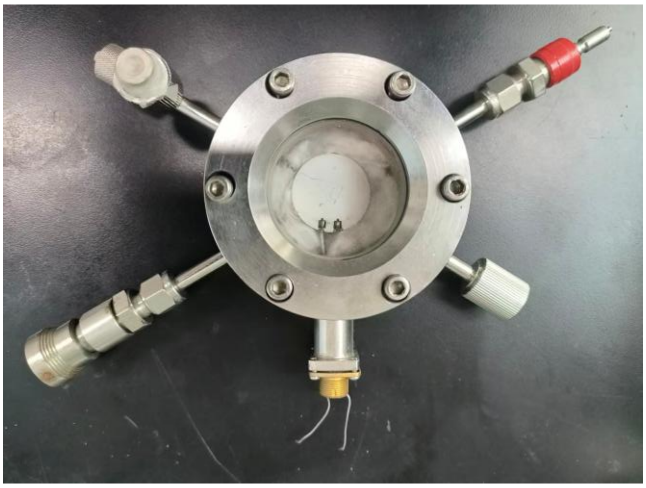

Fig S9. Photograph of home-made reactor for photothermal and thermal catalytic ammonia synthesis.

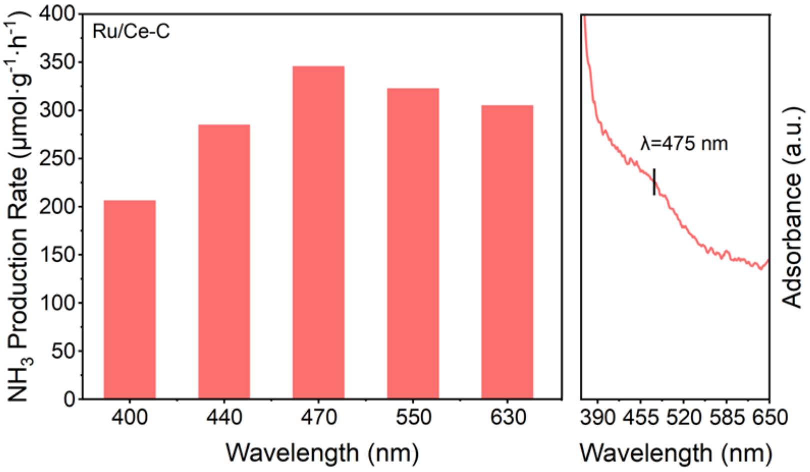

Fig S10. Wavelength-dependent catalytic performance for Ru/Ce-C. Left: UV-Vis absorbance spectrum of Ru/Ce-C.

Note: the wavelength-dependent catalytic performance for Ru/Ce-C exhibits catalytic performance is much lower under 400 nm irradiation even though Ce-C and Ce-R have the maximum absorbance here. Instead, the optimized wavelength is about 470 nm, exhibiting a similar position with the LSPR-induced absorbance of Ru nanoparticle. This result presented catalytic performance increased as the wavelength of irradiation gradually approached to the maximum adsorption peak induced by LSPR of Ru nanoparticle where the dominated photo-excited hot electrons form. It indicates photothermal ammonia synthesis performance was dominated by the photo-excited hot electrons from Ru nanoparticle instead of that from CeO_2 so that the performance became better as the light was more effectively adsorbed by Ru nanoparticle.

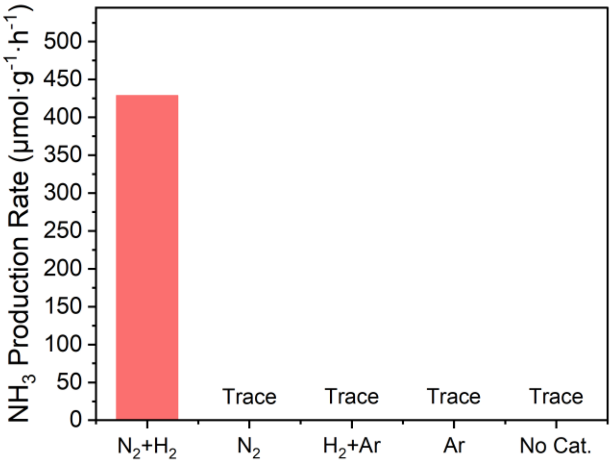

Fig S11. Control experiment for photothermal ammonia synthesis.

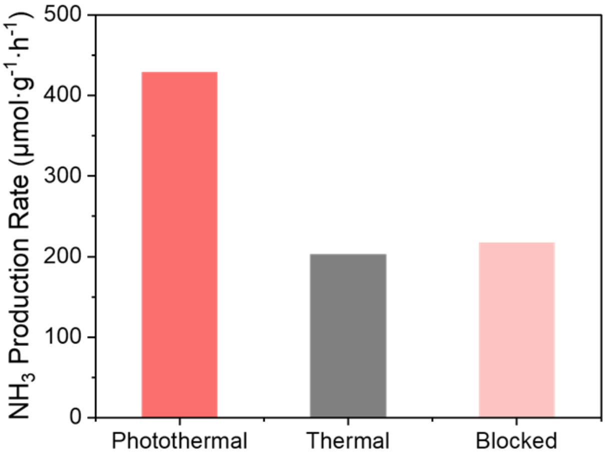

Fig S12. Performance comparison for Ru/Ce-C in photothermal, thermal and Ti_2O_3-blocked conditions.

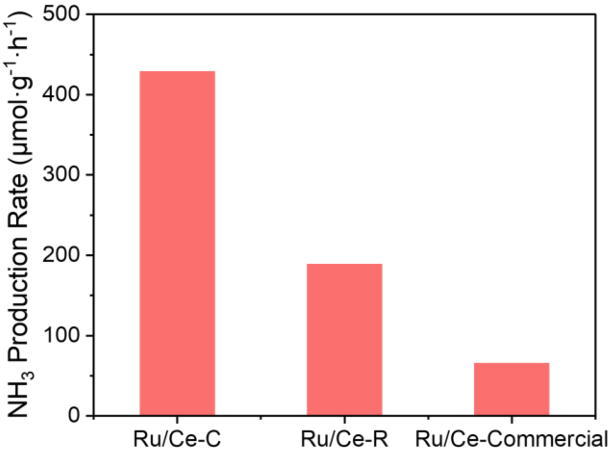

Fig S13. Performance comparison for Ru/CeO_2 catalysts in photothermal condition.

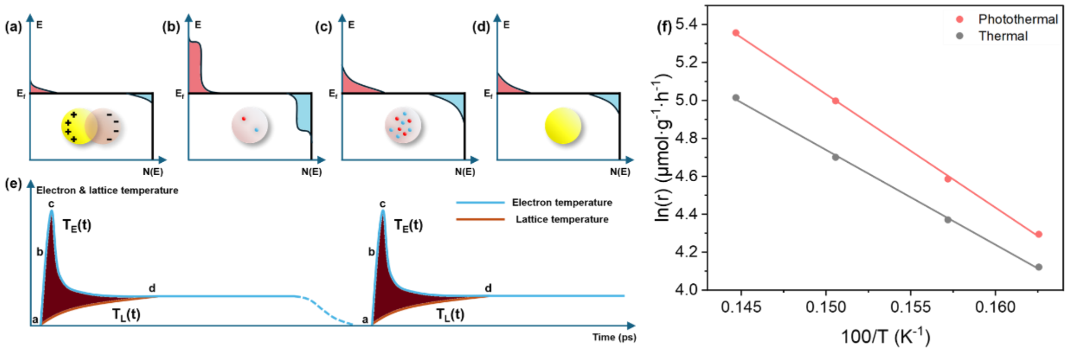

Fig S14. The mechanistic schematic illustrations for LSPR-induced hot electron excitation and relaxation. The states of (a) before plasmon relaxation, (b) after plasmon relaxation and before electron thermalization, (c) after electron thermalization, (d) after equilibrium with a lattice. (f) The Arrhenius plots for Ru/Ce-C under photothermal and thermal conditions. (the calculated apparent activation energy is 140.5 kJ·mol^{-1} for photothermal and 104.34 kJ·mol^{-1} for thermal conditions)

Note: The Arrhenius plots of Ru/Ce-C exhibited a decrease between photothermal and thermal condition (140.5 kJ·mol^{-1} for photothermal condition and 104.34 kJ·mol^{-1} for thermal condition). This may indicate intermediates difference. However, the more significant enhancement , which is induced by the nonequilibrium nature of plasmon-excited hot electron dynamics[17], explains that ammonia synthesis activity was superior under photothermal condition than that under thermal condition. Specifically, the enhanced performance originates from the additional promotion against the electron temperature, which is exhibited as the deep red region in Fig S14 (e).

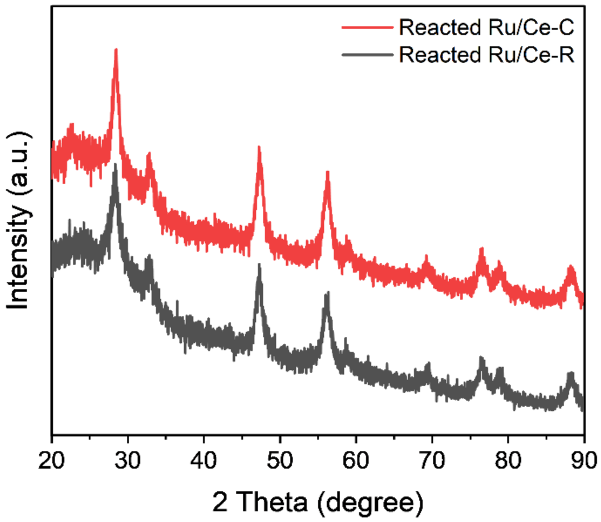

Fig S15. XRD pattern of reacted catalysts.

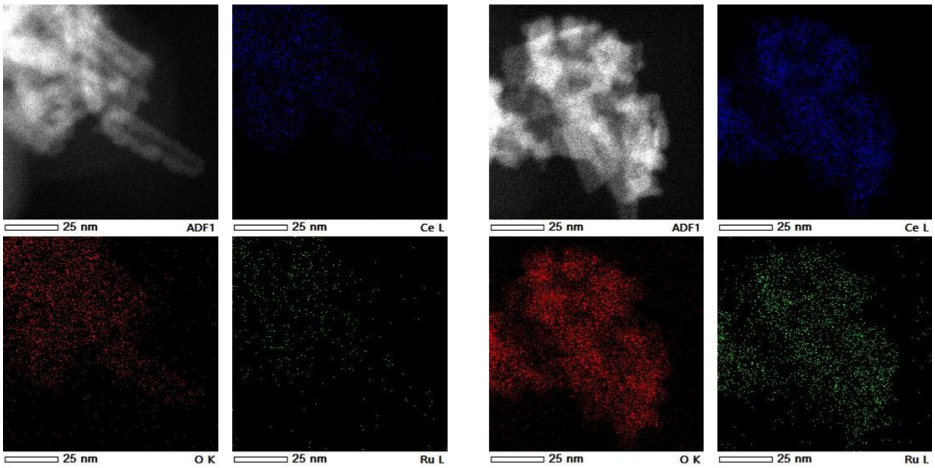

Fig S16. EDX mapping of reacted catalysts.

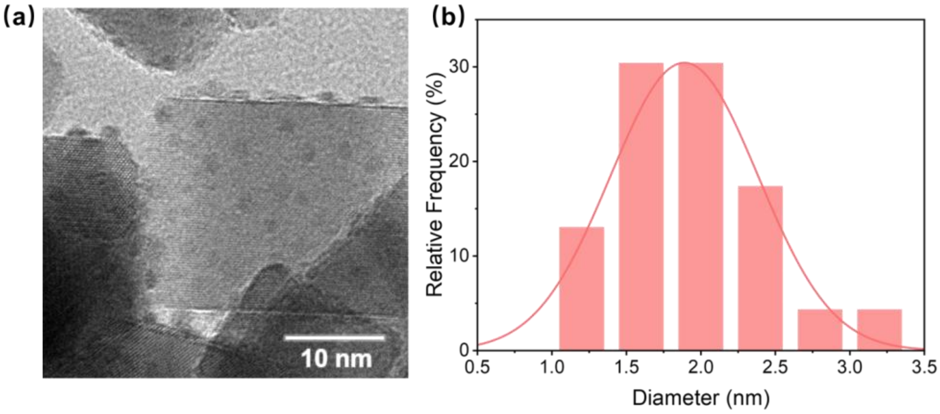

Fig S17. (a) TEM image and (b) the corresponding particle size distribution of Ru nanoparticles.

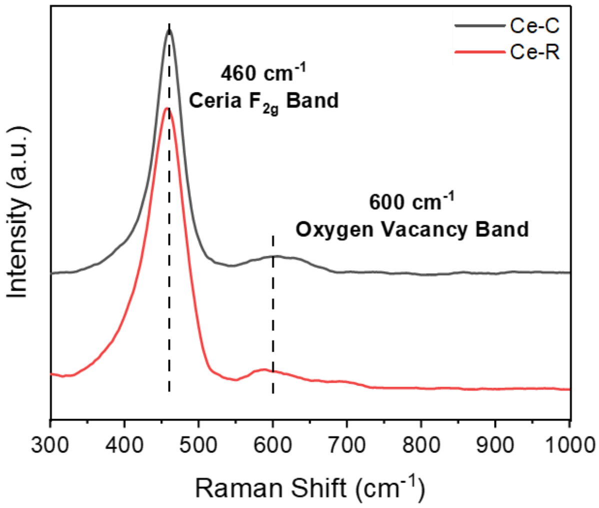

Fig S18. Raman spectra of supports.

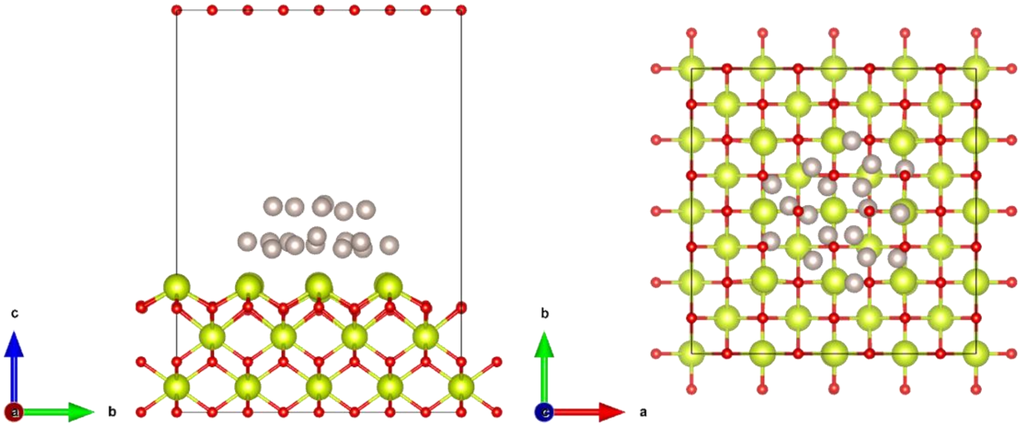

Fig S19. Model of geometric optimized Ru/ceria structure. (left: front view, right: top view, yellow: cerium, red: oxygen, white: ruthenium)

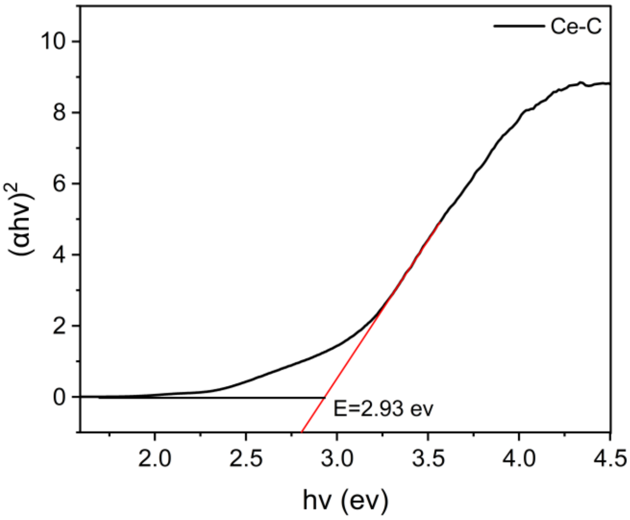

Fig S20. Tauc plot of Ce-C.

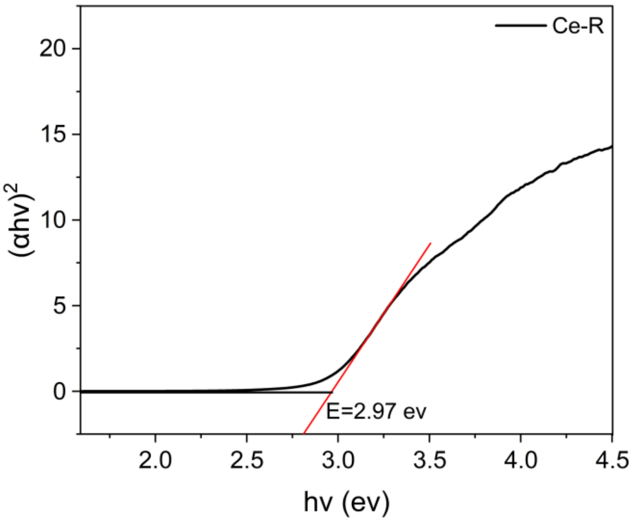

Fig S21. Tauc plot of Ce-R.

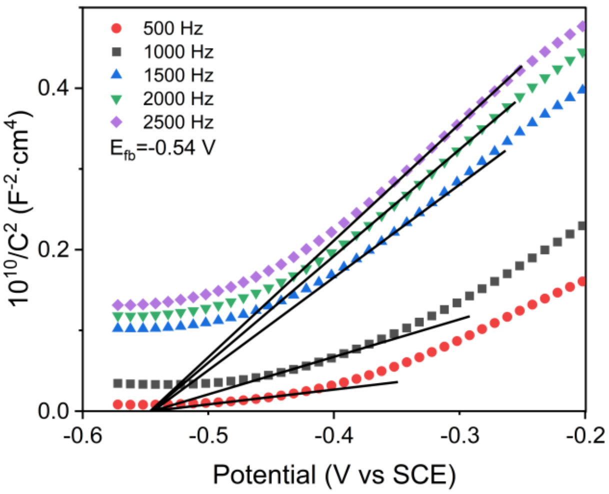

Fig S22. Mott-Schottky plot of Ce-C.

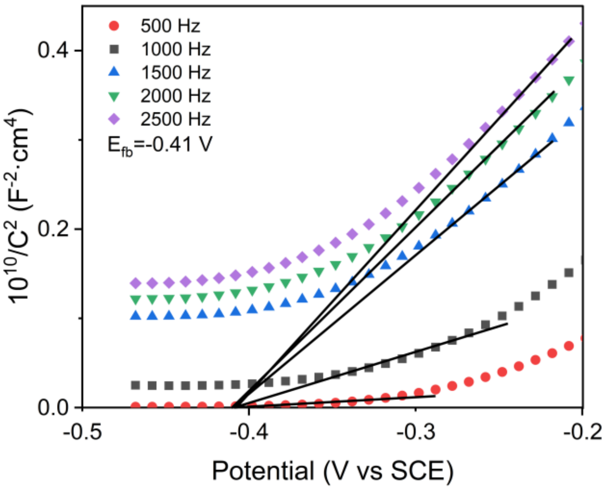

Fig S23. Mott-Schottky plot of Ce-R.

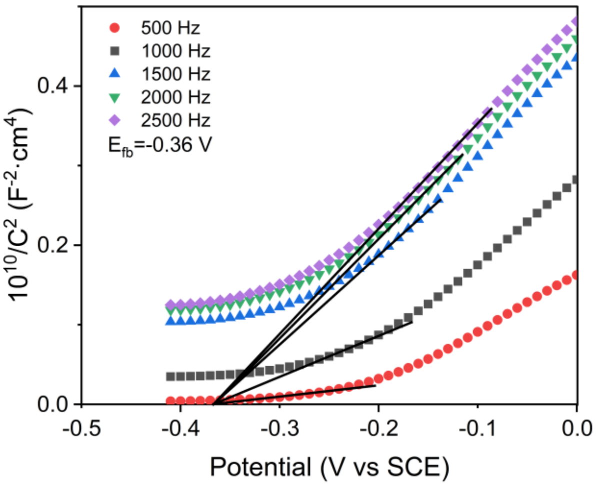

Fig S24. Mott-Schottky plot of Ru/Ce-C.

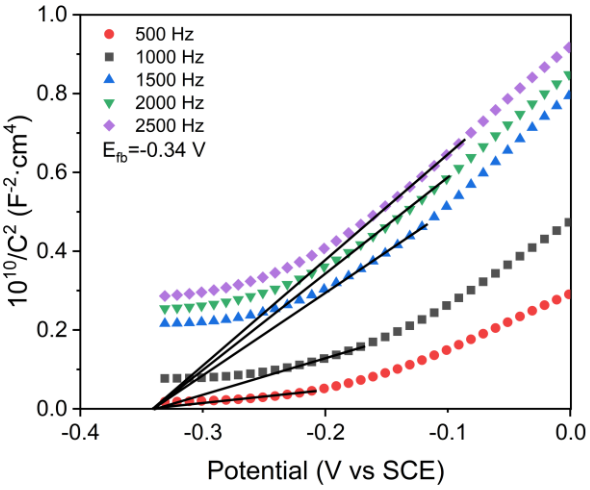

Figure S25. Mott-Schottky plot of Ru/Ce-R.

Note: We measured Mott-Schottky plots using the frequencies ranged from 500-2500 Hz in Fig S22-25. When the frequencies were set as 500, 1000 Hz, the capacitance was dependent on the given frequency. This shows non-ideal behaviour which is possibly related to surface states or interfacial effects and may lead to inaccuracy of extracted flat band potentials. However, when the frequencies were set in the range of 1500-2500 Hz, the capacitance was basically independent with frequency, demonstrating that the extracted flat band potentials under these parameters were reliable.

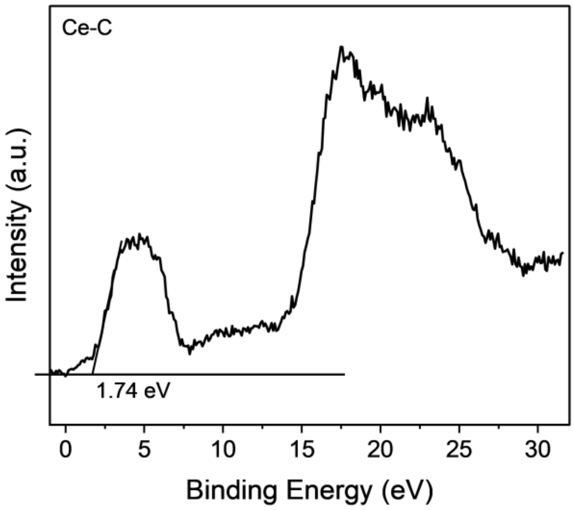

Figure S26. VB-XPS of Ce-C.

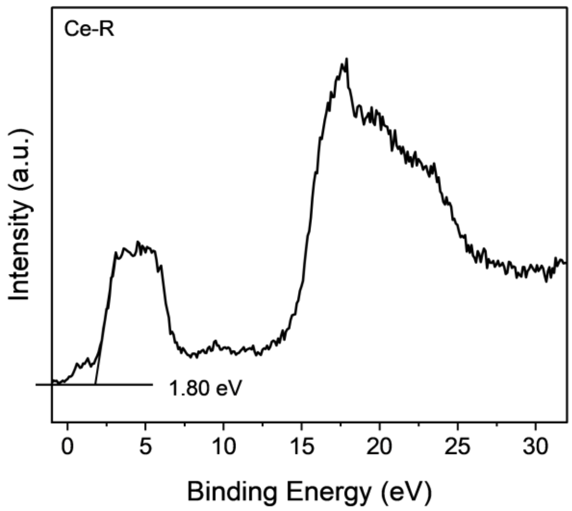

Figure S27. VB-XPS of Ce-R.

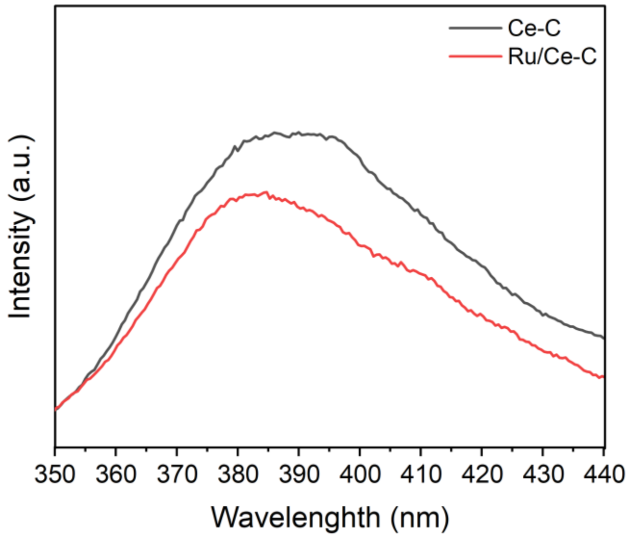

Figure S28. PL spectrum of Ru/Ce-R and Ce-R.

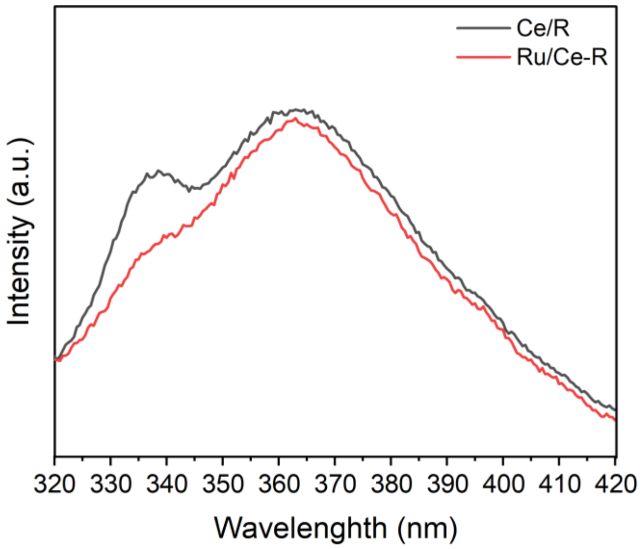

Figure S29. PL spectrum of Ru/Ce-C and Ce-C.

Note: As shown in Figure S28, 29, photoluminescent emission intensity is weaker for both Ru/Ce-R and Ru/Ce-C compared with their corresponding pristine supports. This result exhibits that the construction of heterojunction promotes the separation of photo-excited electron-hole pair and prolongs the lifetime of hot charge carriers.

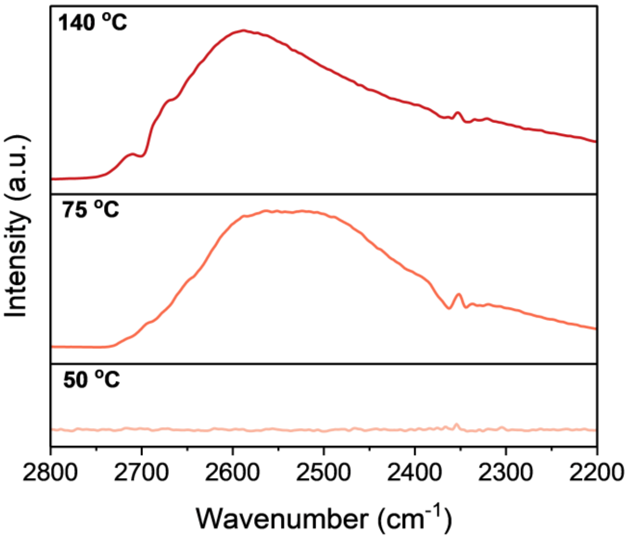

Figure S30. Evolution of DRIFT as temperature rising of Ru/Ce-C.

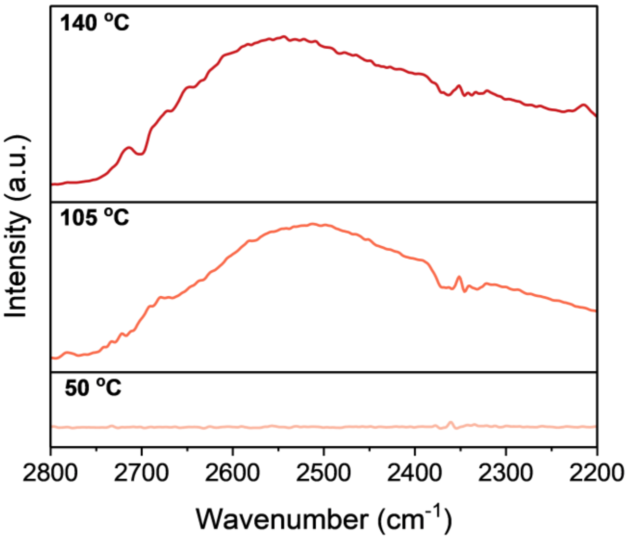

Figure S31. Evolution of DRIFT as temperature rising of Ru/Ce-R.

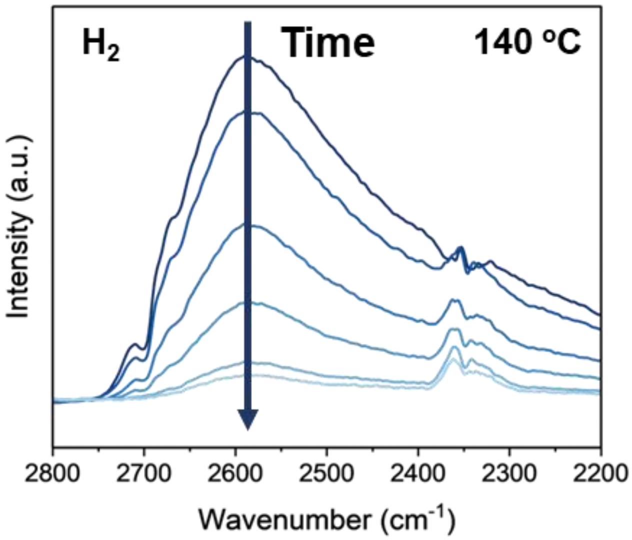

Figure S32. Reversible in-situ DRIFT of H-D exchange experiment of Ru/Ce-C.

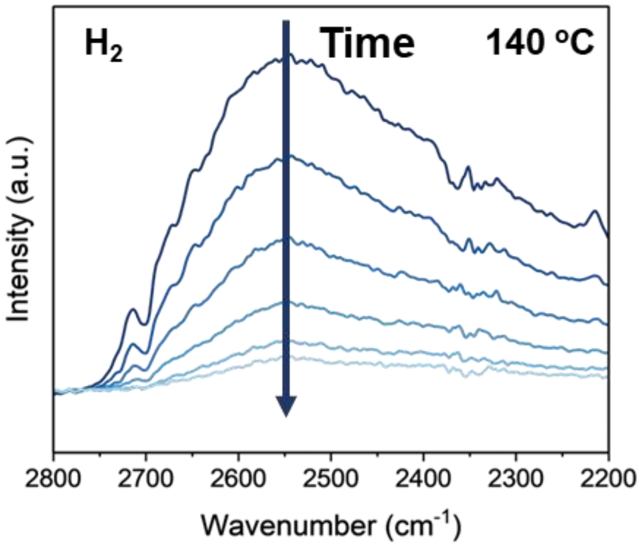

Figure S33. Reversible in-situ DRIFT of H-D exchange experiment of Ru/Ce-R.

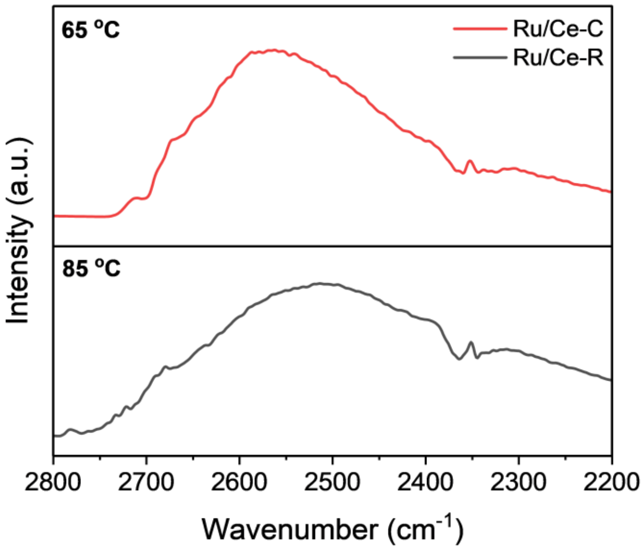

Figure S34. In-situ DRIFT of H-D exchange experiment without light illumination.

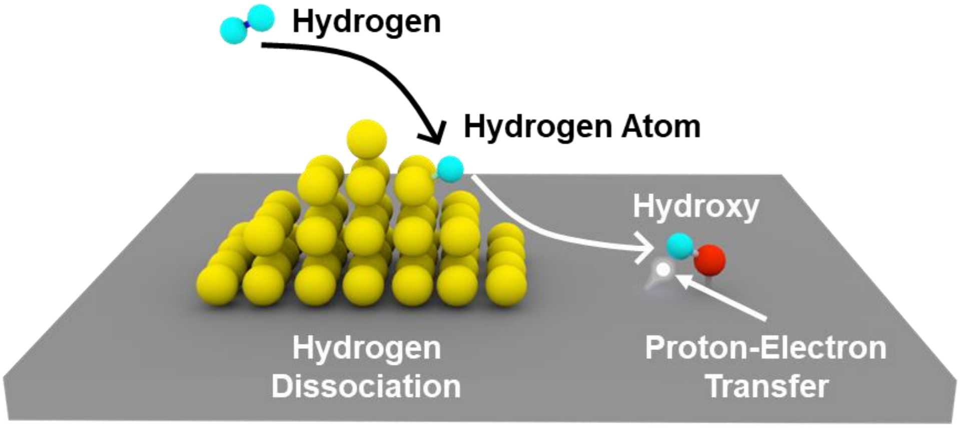

Figure S35. Schematic illustration of hydrogen spillover pathway on reducible support.

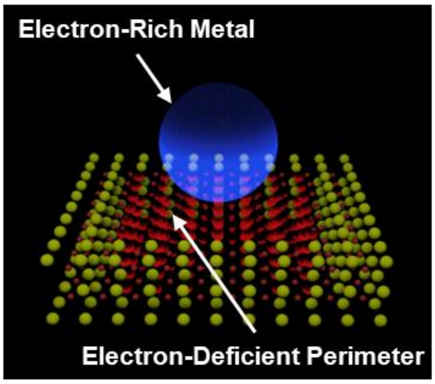

Figure S36. Schematic illustration of electron distribution of catalysts in Dark after metal semiconductor contact.

References

1. X. Chen, D. Shi, M. Bi, J. Song, Y. Qin, S. Du, B. Sun, C. Chen and D. Sun, *J. Colloid Interf. Sci*, 2023, **652**, 653-662.
2. G. Liu, T. Wang, W. Zhou, X. Meng, H. Zhang, H. Liu, T. Kako and J. Ye, *J. Mater. Chem. C*, 2015, **3**, 7538-7542.
3. D. L. Windt, W. C. Cash Jr, M. Scott, P. Arendt, B. Newnam, R. Fisher and A. Swartzlander, *Appl. Opt*, 1988, **27**, 246-278.
4. G. Sharma, R. Verma, S. Masuda, K. M. Badawy, N. Singh, T. Tsukuda and V. Polshettiwar, *Nat. Commu*, 2024, **15**, 713.
5. G. Hass, J. Ramsey and R. Thun, *J. Opt. Soc. Am. A*, 1958, **48**, 324-327.
6. G. Kresse and J. Furthmüller, *Compu. Mater. Sci*, 1996, **6**, 15-50.
7. A. K. Lucid, P. R. Keating, J. P. Allen and G. W. Watson, *J. Phys. Chem. C*, 2016, **120**, 23430-23440.
8. M. J. Zachman, V. Fung, F. Polo-Garzon, S. Cao, J. Moon, Z. Huang, D.-e. Jiang, Z. Wu and M. Chi, *Nat. Commu*, 2022, **13**, 3253.
9. C. Cheng, J. Zhang, R. Zeng, F. Xing and C. Huang, *Appl. Catal. B: Environ*, 2022, **310**, 121321.
10. C. Mao, J. Wang, Y. Zou, Y. Shi, C. J. Viasus, J. Y. Loh, M. Xia, S. Ji, M. Li and H. Shang, *J. Am. Chem. Soc*, 2023, **145**, 13134-13146.
11. L. Yuan, B. B. Bourgeois, E. Begin, Y. Zhang, A. X. Dai, Z. Cheng, A. S. McKeown-Green, Z. Xue, Y. Cui and K. Xu, *Nat. Energy*, 2026, **11**, 98-108.
12. J.-Z. Qiu, J. Hu, J. Lan, L.-F. Wang, G. Fu, R. Xiao, B. Ge and J. Jiang, *Chem. Mater*, 2019, **31**, 9413-9421.
13. Y. Peng, J. Albero, A. Franconetti, P. Concepción and H. García, *ACS Catal*, 2022, **12**, 4938-4946.
14. Y. Yang, C. Li, X. Yang, S. Chen, Y. Gong and J. Wang, *Chem. Eng. J*, 2026, **530**, 173538.
15. M. Kikugawa, Y. Goto, K. Yamazaki, Y. Manaka, T. Nanba, H. Matsumoto, A. Sato and M. Aoki, *Appl. Catal. A: Gen*, 2025, 120525.
16. Y. Bai, Y. Zhang, J. Hu, J. Li, S. Wan, J. Lin, Y. Wang and S. Wang, *ACS Catal*, 2025, **15**, 1455-1466.
17. J. Khurgin, A. Y. Bykov and A. V. Zayats, *Elight*, 2024, **4**, 15.